



OPEN

High accuracy capillary network representation in digital rock reveals permeability scaling functions

Rodrigo F. Neumann¹, Mariane Barsi-Andreeta², Everton Lucas-Oliveira², Hugo Barbalho^{1,4}, Willian A. Trevisan³, Tito J. Bonagamba² & Mathias B. Steiner¹

Permeability is the key parameter for quantifying fluid flow in porous rocks. Knowledge of the spatial distribution of the connected pore space allows, in principle, to predict the permeability of a rock sample. However, limitations in feature resolution and approximations at microscopic scales have so far precluded systematic upscaling of permeability predictions. Here, we report fluid flow simulations in pore-scale network representations designed to overcome such limitations. We present a novel capillary network representation with an enhanced level of spatial detail at microscale. We find that the network-based flow simulations predict experimental permeabilities measured at lab scale in the same rock sample without the need for calibration or correction. By applying the method to a broader class of representative geological samples, with permeability values covering two orders of magnitude, we obtain scaling relationships that reveal how mesoscale permeability emerges from microscopic capillary diameter and fluid velocity distributions.

Permeability is a critical figure-of-merit in the characterization of porous geological samples for applications ranging from water management to fluid recovery and carbon dioxide sequestration^{1–8}. Fluid flow assessment in rocks typically involves multiple physical length scales; a fluid passes through a complex, interconnected network of capillaries with diameters ranging from nanometers to millimeters, while flow conditions are typically set and measured at lab scale, see Fig. 1. Once the spatial distribution of the connected pore space in a rock sample is known, a flow model is applied to computationally predict the fluid permeability based on the capillary network geometric boundaries^{9–14}. We show in the following that a high-accuracy, network-based representation of a microscopic fraction of a rock's connected pore space is a suitable template for computationally predicting experimental permeability results obtained from the same rock sample at lab scale, a volume upscaling by 3 orders of magnitude. An application of the method to 11 sandstone samples, see Table 1, reveals permeability scaling as function of diameter distribution and flow speed. We suggest that the extracted slopes be used more generally for characterizing permeability scaling in this geological sample class.

Methodically, the application of X-ray microtomography to rock samples provides a series of images of the spatial distribution of the pore space from which three-dimensional digital rock representations are created^{16–18}. Once a full series of microscopic rock images is acquired, the image series undergoes a sequence of processing steps with regards to noise, segmentation and morphology, producing a data cube (digital rock) containing voxels that either represent solid or void space of the imaged rock¹⁹. Here, the spatial discretization method—such as meshes and grids, used by Finite-Element, Finite-Volume and Lattice Boltzmann; or nodes and edges, used by network-based methods—depends on the flow simulation algorithm to be used for performing subsequent permeability predictions^{20–25}. Mesh and grid-based numerical methods have the advantage of being more adaptable—to within the size of the voxel—to the geometry of the pore space¹⁷. However, the requirement to fill the entire pore space with either mesh elements or grid points makes these methods less computationally efficient^{20,25}. Network-based models, on the other hand, balance geometrical accuracy and computational complexity by representing pore space through geometrical primitives, e. g. cylinders and spheres, for which flow properties are typically obtained in (semi-) analytical form^{14,20,24}.

¹IBM Research, Rio de Janeiro, RJ 22290-240, Brazil. ²São Carlos Institute of Physics, University of São Paulo, PO Box 369, São Carlos, SP 13560-970, Brazil. ³CENPES/Petrobras, Rio de Janeiro, RJ 21941-915, Brazil. ⁴Present address: Dell Technologies, Rio de Janeiro, RJ 21941-907, Brazil. ✉email: rneumann@br.ibm.com; mathiast@br.ibm.com

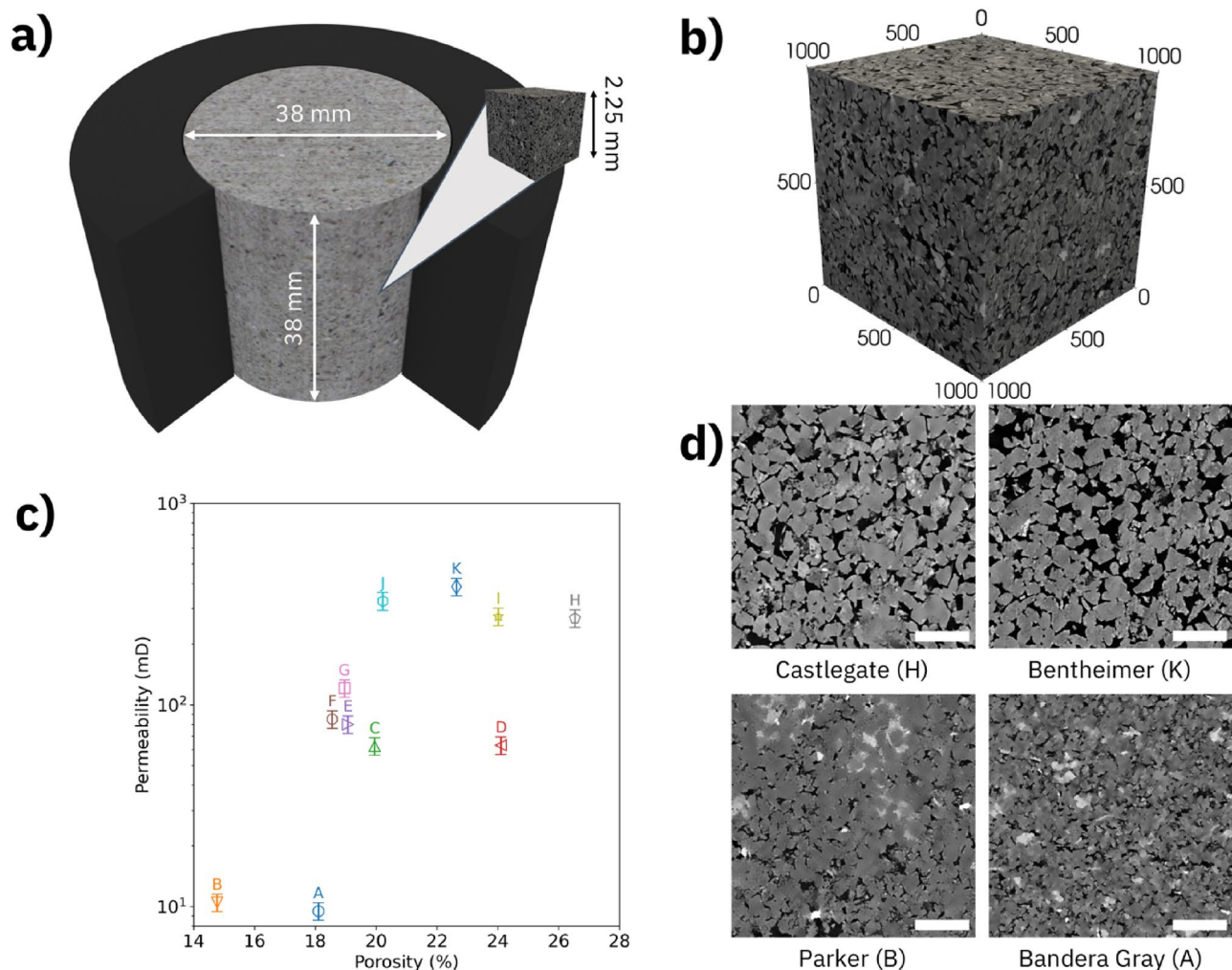


Figure 1. Conception of permeability and porosity determination in rock samples. (a) Permeability and porosity measurements are performed at lab scale. However, computational simulations are performed with microscopic network representation at pore scale. 3D visualization created using Blender v2.92.0 software. (b) Pore scale representation of a rock sample derived from an X-ray microtomography with 1000 voxels of 2.25 μm along each side, resulting in an overall side length of 2.25 mm. 3D visualization created using ParaView v5.9.0 software. (c) The experimental porosity–permeability plot of containing all rock samples. (d) Representative grayscale images extracted from the data cube of the least porous (B), least permeable (A), most porous (H) and most permeable (K) rock sample, respectively, exhibit the microstructural variation occurring at pore scale. The white scale bar at the lower right corner of each image represents 500 μm .

Sample	Name	Porosity (%)	Permeability (mD)
A	Bandera Gray	18.10	9
B	Parker	14.77	10
C	Kirby	19.95	62
D	Bandera Brown	24.11	63
E	Berea Sister Gray	19.07	80
F	Berea Upper Gray	18.56	86
G	Berea	18.96	121
H	Castlegate	26.54	269
I	Buff Berea	24.02	275
J	Leopard	20.22	327
K	Bentheimer	22.64	386

Table 1. List of sandstone rock samples used in our study and their respective properties. Sample labels A–K are listed in increasing order of permeability. We estimate the experimental error to be $\pm 0.5\%$ for porosity and $\pm 10\%$ for permeability, respectively¹⁵.

In any of these methods, the tradeoff between the voxel (volume pixel) size and the total imaged sample volume poses practical limits to the spatial resolution of lab scale samples in which permeability measurements are typically performed. The computational representations of lab scale rock sample do not fully resolve the diameter distribution of the capillary network, which consequently leads to inaccuracies in permeability predictions. In addition, computational approximations of the connected pore space by geometrical primitives, such as balls and sticks, can be insufficient to capture the actual complexity of the capillary network at pore scale. Sample heterogeneities can further complicate the picture; the higher the spatial heterogeneity of a rock sample the larger the Representative Elementary Volume (REV) for quantifying the threshold sampling volume at which the statistical properties of the capillary network become representative for the entire lab scale rock sample^{26–29}. In essence, a combination of stringent requirements needs to be met for successfully predicting the permeability of lab scale samples based on microscopic capillary network representations.

For establishing those requirements, we have systematically analyzed a representative group of highly resolved, three-dimensional microscopic image cubes measured on rock samples for which permeability and porosity have been experimentally verified at lab scale. For evaluating the influence of pore scale representation quality on the accuracy of permeability predictions, we have used three candidate network representations with varying levels of spatial detail as geometrical template: (1) the *Capillary Network Model* (CNM), which transforms the pore space into a voxel-wide line at the center of the pore channels; (2) the *Reduced Max Ball Model* (RMB)³⁰, in which the network is constructed using connecting cylinders modelled by longer line segments that follow the medial axis of the pore space; and (3) the *Pore Network Model* (PNM)³¹, which divides pore space into pores and throats, where each pore is a node in the network and each throat is a link between nodes. For each sample, we have compared the computational permeability predictions obtained for each of the three pore space representations with the experimental permeability obtained from the same rock sample at lab scale. By aggregating the data of all samples studied, we have obtained the scaling relationships and slopes for characterizing more broadly the permeability of the entire sandstone sample class.

Results

Experimental characterization. We have measured the porosity and permeability of a set of 11 cylindrical sandstone samples with radii and heights of 19 and 38 mm, respectively. The connected porosities found in these samples range from 14 to 27%, with a mean of $20 \pm 3\%$, and the absolute permeabilities from 9 to 386 mD, with a mean of 150 ± 40 mD, as summarized in Table 1. Details on the flow measurements are provided in the “Methods” Section. In Fig. 1c, we plot the measured gas permeability and porosity for each sample. The microscopic distributions of connected pore space in each rock are mainly responsible for the observed porosity/permeability variations as can be examined by visual inspection of the X-ray microtomography images of the samples. In Fig. 1d, we show representative images taken at the center of the image cube of the least porous (B), least permeable (A), most porous (H) and most permeable (K) rock samples in the dataset.

We have acquired X-ray microtomography image cubes on sub-samples (height = 30 mm, radius = 5 mm) extracted from each of the rock plugs listed in Table 1 (see “Methods” Section for details). The representative three-dimensional microtomography in Fig. 1b has a voxel size of $2.25 \mu\text{m}$ in which the lighter (darker) gray levels correspond to solid (void) space in the sandstone. For extracting the connected pore space, we have processed each raw image (gray scale) cube through a workflow that includes contrast-enhancement, noise reduction and threshold-based segmentation (see “Methods” Section for details). The resulting binary image cube contains the spatial map of pore space inside the sample. The volume fraction of voxels identified as pores is readily available, however, a subsequent processing step is needed to remove isolated pores that do not contribute to permeability.

We have then used the connected pore space in the image cube as a template for performing numerical flow simulations and permeability predictions. By analyzing the dependence of flow simulation accuracy on rock image cube size, see Supplementary Figure S2, we obtain $\text{REV} = (2.25 \text{ mm})^3$. Finally, we obtain a volume scaling factor of $V_{\text{exp}}/\text{REV} = 3784$, which relates the connected pore space volume used for computing permeability predictions to the reference sample volume that we have probed in our lab experiments.

Numerical simulations. For quantifying the accuracy of geometric approximation in the digital rocks, we have compared three network-based representations of the microscopic pore space—PNM as algorithmically implemented in the PoreSpy open-source package³², RMB based on the algorithm developed by Andreetta et al.³⁰ and CNM performed by an algorithm reported here for the first time. The particular choice of candidate network representations maps the spectrum of network models in terms of spatial detail, from PNM (coarse) via RMB to CNM (fine).

In Fig. 2, we show pore network (top) and capillary network (bottom) representations applied to the same sample region. In a pore network representation, see Fig. 2a, the void space is sub-divided into pores and throats. Pore and throat are each represented by their radius, R_p and R_t , respectively, while specifics of the cross-sectional geometries are matched using shape factors¹⁴. In Fig. 2b, a network of spheres and cylinders geometrically approximates the occurring void space. For comparison, Fig. 2c exemplifies how a capillary network representation would approximate the same sample region. Here, the void space is filled with short (one voxel long) cylinders having their radii $\{R_n\}$ evolving gradually to match the local boundaries. The resulting network of connected capillaries in this approximation is shown in Fig. 2d.

In PNM, nodes are associated with pores, which have a finite volume, and links are associated with throats, which impose a resistance to the flow between the two nodes it connects. In CNM, on the other hand, nodes are considered zero-volume points that do not contribute to the pore space, while links represent finite-volume cylinders that account for all the pore volume and flow resistance. Finally, RMB has features of both pore and capillary network representations as it uses extended cylinders to represent the pore space.

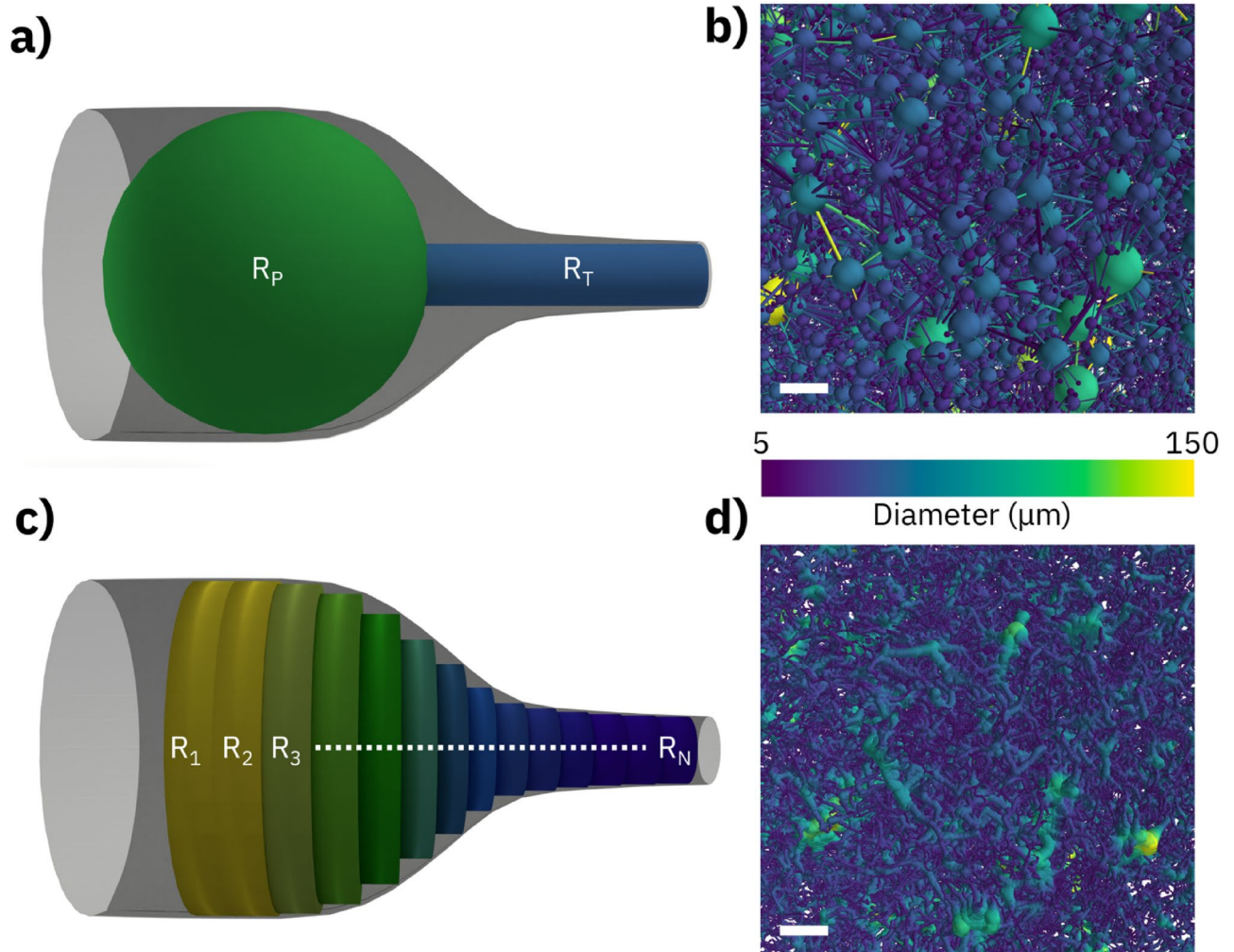


Figure 2. Visual conceptions (left) and implementation examples (right) of representative network models. **(a)** The Pore Network Model separates the pore space into spherical pores with radius R_P and cylindrical throats with radius R_T . **(b)** Pore Network Model representation using color-coded diameters. **(c)** The capillary network model separates the pore space into a sequence of short cylinders with gradually changing radii $\{R_n\}$. **(d)** Capillary Network Model representation using color-coded diameters. The white scale bar represents 100 μm . Visual conceptions **(a,c)** created using Blender v2.92.0 software.

In Fig. 3, we have compared the experimental and computational porosities and permeabilities. The computational porosity values extracted from the connected pore space in digital rocks are plotted against the experimental porosity values in Fig. 3a. The diagonal indicating a perfect match between experiment and computational prediction is overlaid by a gray shaded area indicating a root mean squared error of 2.25%. Nine of eleven samples fall within the shaded area, indicating reasonable agreement.

In Fig. 3b, we plot the experimental and simulated permeabilities for each network model considered in this study. In each of the three network representations, we have simulated water flow assuming a 10 kPa/m pressure gradient across the sample. The flow simulation algorithm solves a linear system of equations that applies Poiseuille law at each network link (i.e., cylindrical capillary) and mass conservation law at each network node (for details see “Methods” Section). The simulated data points represent the quadratic mean of the simulated permeability along the three main axes. Considering the entire sandstone sample set, we observe the best agreement for CNM with a mean relative error between model prediction and experimental result of 38%, followed by RMB with 42%, attesting to the high accuracy of the geometrical approximation achieved with this approach. In contrast, the PNM based predictions are significantly less accurate, at a mean relative error of 92%, with a maximum mismatch of more than a factor of two in the case of sample K. In all cases, the agreement between simulated and experimental permeabilities decreased for higher permeability samples, as previously reported²⁵.

As a key result of this investigation, we plot in Fig. 4, for each sample, the relationship between lab scale permeability and microscopic properties based on CNM. While bulk permeability and porosity of the sample class are broadly scattered, see Fig. 1, the permeability (both experimental and computed) scales with the mean capillary diameter observed in the samples, see Fig. 4a. A linear fit to the data provides a slope of $(0.098 \pm 0.007) D[\mu\text{m}]$ for $\log_{10} K[\text{mD}]$, which characterizes the entire sandstone sample set. In Fig. 4b, we plot experimental

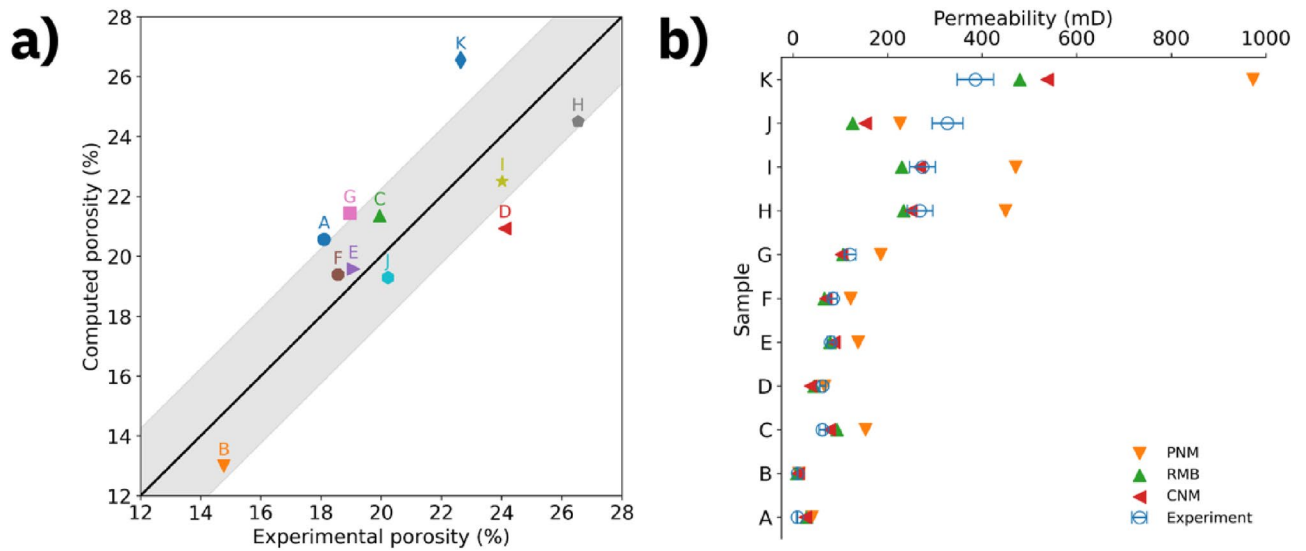


Figure 3. Comparison between experimental and computed porosities and permeabilities. (a) Computed versus experimental porosity for all samples studied. The solid line indicates agreement between computation and experiments and the gray shaded area represents the root mean squared error of 2.25 percentage points. (b) Experimental and simulated permeability for all samples studied. The computational results represent the mean permeability along the three main axes. Experimental results are represented by (blue) open circles, those from the Pore Network Model by (orange) filled down-pointing triangles, those from the Reduced Max Ball Model by (green) filled up-pointing triangles and those from the Capillary Network Model by (red) filled left-pointing triangles.

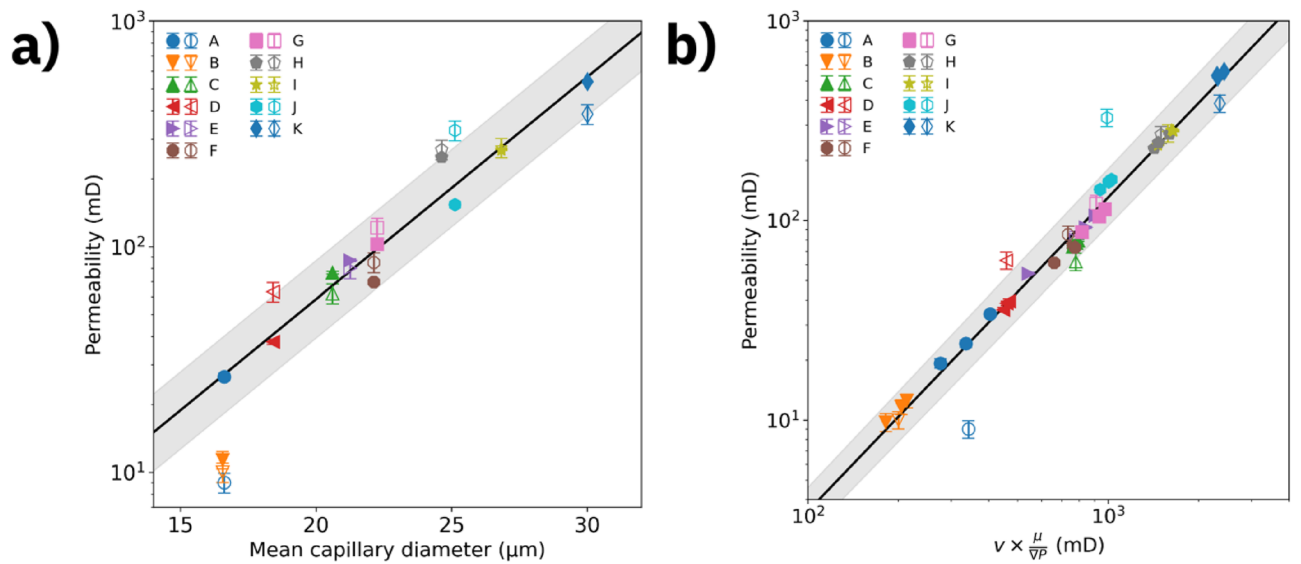


Figure 4. Scaling of permeability as function of mean capillary diameters and mean flow speeds. Computed (experimental) permeability is represented by filled (open) symbols. (a) Permeability as function of mean capillary diameter for all rock samples studied. (b) Permeability as function of volume-averaged flow speed multiplied by $(\mu/\nabla P)$ along all 3 axes for all rock samples studied. The plot aggregates results from simulation scenarios with viscosity $\mu = 1$ cP and pressure gradient of 10 kPa/m, as well as variations with 10× higher viscosity or 10× stronger gradient, covering two orders of magnitude variation in flow speeds. The lines represent linear fits to the data and the shaded area represents the fit uncertainty. The computed data are CNM results.

and computed permeability as a function of generalized velocity $u = (v \times \mu/\nabla P)$, where v is the (microscopic) volume-weighted average flow speed inside the capillaries, μ is the dynamic viscosity of the fluid and ∇P is the pressure gradient along the flow axis. A linear fit to the data ($R^2 > 0.98$) in a $\log_{10} K[\text{mD}] \times \log_{10} u[\text{mD}]$ plot of indicates that permeability is well-described by $(0.0024 \pm 0.0003) \times u^{1.57 \pm 0.02}$ for the entire set of sandstone samples.

A practical application of the scaling results is estimating lab scale permeabilities based on mean capillary diameters and flow speeds taken from CNM predictions performed on X-ray microtomography data or, conversely, getting insight into microscopic flow speeds based on lab scale permeability measurements.

Discussion

We have computationally predicted lab scale permeabilities based on X-ray microtomography data for a sample set containing 11 sandstones. For performing fluid flow simulations, we have used three network-based geometrical representations of a microscopic volume fraction of the connected pore space of a rock. The representation with the highest level of spatial detail, CNM, enables predicting experimental permeability results obtained from the same rock sample at lab scale (more than 3000 × volume) with a mean relative error between microscopic model prediction and lab scale experimental result of 38%. By aggregating the results, we have obtained scaling relationships between the lab scale permeabilities and the mean capillary diameter and flow speed, respectively, for the sandstone sample class that can be used for estimating lab scale permeabilities based on X-ray microtomography data. These results demonstrate the relationship between accuracy of microscopic detail employed by the network representation and the scaling potential of the ensuing permeability calculation. Future research should extend the above methodology to geological sample classes with higher degrees of heterogeneity and more complex capillary diameter distributions, such as carbonate and shale rocks. The extension of the work to these rock types will likely require smaller voxels and larger sampling volumes, which is expected to increase the computational cost of network-based methods, but still less than the expected cost increase for mesh- and grid-based methods.

Materials and methods

Rock samples. We have acquired a set of sandstone rocks (*Kocurek Industries INC.*) with the following 11 samples: Bandera Gray (A), Parker (B), Kirby (C), Bandera Brown (D), Berea Sister Gray (E), Berea Upper Gray (F), Berea (G), Castlegate (H), Buff Berea (I), Leopard (J) and Bentheimer (K).

Lab permeability measurement. We have experimentally characterized the cylindrical plug samples (height = 38 mm, radius = 19 mm) at lab scale following the API RP-40 norm³³. In a first step, we have measured porosity through Helium pressure variations in a Boyle's Law Double Cell. In a second step, we have measured permeability by monitoring steady-state Nitrogen flow rate in the axial direction of the cylindrical samples³⁴. We have applied an axial pressure gradient of 30–40 psi to the samples for establishing laminar flow conditions. For restricting fluid flow to the axial direction, we have confined the plugs laterally by applying a radial pressure through a rubber sealing. We have limited the radial pressure to 500 psi so to avoid significant modifications of the plug's pore volume. Finally, we have applied a Klinkenberg correction³⁵ to correct for fluid expansion. We estimate the experimental error to be ± 0.5% for porosity and ± 10% for permeability, respectively¹⁵.

X-ray microtomography. In a next step, we have sub-sampled the plugs to obtain smaller cylindrical samples (height = 30 mm, radius = 5 mm). We have obtained pore scale image data by using high-resolution 3D X-ray Microtomography (SkyScan 1272, Bruker). We have set source voltage and current to 50 kV and 200 μA, respectively. We have configured the CCD camera to acquire projections of 4904 × 3280 pixels, resulting in a pixel side length of 2.25 μm. We have performed image reconstruction using SkyScan NRecon (version: 1.7.0.4, Bruker).

Image processing. We have processed the rock image data into subsets containing 1000³ cubic voxels and converted the image from 16-bit to 8-bit gray scale. We have then applied an enhancement filter to equalize the contrast across multiple images. For each data set, we have cut off the grayscale level where the accumulated grayscale histogram achieved 99.8% and mapped the remaining grayscale levels to the [0, 255] interval. To reduce image noise, we have executed on each data set a 3D non-local means filter^{36,37} available in Fiji³⁸ using a smoothing factor of 1 and automatically estimated sigma³⁹ parameters. Finally, by using a threshold level calculated by the IsoData method⁴⁰, we have segmented the noise-reduced grayscale images into solid and void space leading to a binary image. The image-processing parameters for each sample are available in Supplementary Table S1. We have then processed the binary images using the Enhanced Hoshen-Kopelman algorithm⁴¹ for morphological analysis and, in a final step, eliminated from each data cube the pore voxels that are not connected to the percolating network.

Network extraction. We have then used the binary image data sets containing the connected pore voxels as input to three representative network extraction algorithms: PNM, RMB and CNM. Briefly, all algorithms calculate distance maps of the images and construct a hierarchical graph of the voxels associated with the void space.

The PNM is extracted using the SNOW algorithm based on watershed transformation³¹, available in PoreSpy³² version 1.2.0, which is specialized in extracting pore networks from high-porosity materials.

The RMB algorithm³⁰ is a modified medial-axis extraction based on the original Max Ball Algorithm. The pore-throat connections in the Max Ball Algorithm are found through the maximum ball chains. These chains are further processed in the RMB by finding the optimum fluid flow paths between pore centers through Dijkstra's algorithm. The final output is a simplified medial axis composed by the spheres on the optimum paths' chains. The sphere's centers are the nodes in the network and the links are modelled by the neighboring spheres radii and distance between centers.

The CNM representation is based on the *Centerline* algorithm⁴². A centerline is a thin, one-dimensional object that captures a 3D object's main symmetry axes, summarizing its main shape into a set of curves⁴³. In this work, we have used for the first time an algorithm that extracts the centerlines of a 3D image by using an adaptation of the traditional Dijkstra's Minimum Path algorithm in a graph with penalized distance. The full algorithm description can be found in the Supplementary Information.

Flow simulation. The flow simulation algorithm applied in this study operates on nodes and links of the network representations. Specifically, the algorithm applies Poiseuille law to the links and mass conservation law to the interior nodes, while maintaining a fixed pressure difference between inlet and outlet boundary nodes. This is represented by a system of mass conservation equations $\sum_j Q_{ij} = 0$ for all nodes i , where $Q_{ij} = (\pi R_{ij}^4 / 8\mu L_{ij}) (P_i - P_j)$ is the flow rate in the capillary that connects node i to node j . The geometrical parameters R and L , respectively, represent the radius and the length of a capillary (link) connecting two nodes of the network and μ is the dynamic viscosity of the fluid. Unless stated otherwise, all simulations used a viscosity of $\mu = 1$ cP and applied a 10 kPa/m pressure gradient along the flow direction in addition to atmospheric pressure. We have calculated permeability using Darcy's Law $Q = K (A/\mu L) \Delta P$, which causes μ and ΔP to factor out and not affect the results. In order to validate the flow simulations, we have benchmarked them against OpenPNM⁴⁴ version 2.4.2, with results matching within ± 1 mD.

Data availability

The microtomography datasets generated and/or analyzed during the current study are available in the Digital Rocks Portal repository, at <https://dx.doi.org/10.17612/f4h1-w124>.

Code availability

The code used to obtain the PNM results reported in the current study are available in a Github repository, at https://github.com/mbandreeta/absolute_permeability_simulations.

Received: 30 October 2020; Accepted: 30 April 2021

Published online: 15 June 2021

References

1. Su, E., Liang, Y., Zou, Q., Niu, F. & Li, L. Analysis of effects of CO₂ Injection on coalbed permeability: implications for coal seam CO₂ sequestration. *Energy Fuels* **33**, 6606–6615 (2019).
2. Niu, Q. & Zhang, C. Permeability prediction in rocks experiencing mineral precipitation and dissolution: a numerical study. *Water Resour. Res.* **55**, 3107–3121 (2019).
3. Zhang, P., Celia, M. A., Bandilla, K. W., Hu, L. & Meegoda, J. N. A pore-network simulation model of dynamic CO₂ migration in organic-rich shale formations. *Transp. Porous Media* **133**, 479–496 (2020).
4. Al-Janabi, A. M. S., Yusuf, B. & Ghazali, A. H. Modeling the infiltration capacity of permeable stormwater channels with a check dam system. *Water Resour. Manag.* **33**, 2453–2470 (2019).
5. Millington, R. & Quirk, J. P. Permeability of porous solids. *Trans. Faraday Soc.* **57**, 1200–1207 (1961).
6. Yu, X., Hong, C., Peng, G. & Lu, S. Response of pore structures to long-term fertilization by a combination of synchrotron radiation X-ray microcomputed tomography and a pore network model. *Eur. J. Soil Sci.* **69**, 290–302 (2018).
7. Roth, K. Fluids in porous media. *Soil Phys.* **3**, 39–67 (2012).
8. Berg, C. F. & Held, R. Fundamental transport property relations in porous media incorporating detailed pore structure description. *Transp. Porous Media* **112**, 467–487 (2016).
9. Zheng, D. & Reza, Z. Pore-network extraction algorithm for shale accounting for geometry-effect. *J. Pet. Sci. Eng.* **176**, 74–84 (2019).
10. Liang, Y., Hu, P., Wang, S., Song, S. & Jiang, S. Medial axis extraction algorithm specializing in porous media. *Powder Technol.* **343**, 512–520 (2019).
11. Rabbani, A., Mostaghimi, P. & Armstrong, R. T. Pore network extraction using geometrical domain decomposition. *Adv. Water Resour.* **123**, 70–83 (2019).
12. Silin, D. & Patzek, T. Pore space morphology analysis using maximal inscribed spheres. *Phys. A Stat. Mech. its Appl.* **371**, 336–360 (2006).
13. Arand, F. & Hesser, J. Accurate and efficient maximal ball algorithm for pore network extraction. *Comput. Geosci.* **101**, 28–37 (2017).
14. Raeini, A. Q., Bijeljic, B. & Blunt, M. J. Generalized network modeling: Network extraction as a coarse-scale discretization of the void space of porous media. *Phys. Rev. E* **96**, 1–17 (2017).
15. Thomas, D. & Pugh, V. A statistical analysis of the accuracy and reproducibility of standard core analysis. *Petrophysics* **30**, 71–77 (1989).
16. Saxena, N., Hows, A., Hofmann, R., Freeman, J. & Appel, M. Estimating pore volume of rocks from pore-scale imaging. *Transp. Porous Media* **129**, 403–412 (2019).
17. Saxena, N. *et al.* Effect of image segmentation & voxel size on micro-CT computed effective transport & elastic properties. *Mar. Pet. Geol.* **86**, 972–990 (2017).
18. Cnudde, V. & Boone, M. N. High-resolution X-ray computed tomography in geosciences: a review of the current technology and applications. *Earth-Science Rev.* **123**, 1–17 (2013).
19. Andrä, H. *et al.* Digital rock physics benchmarks—part I: imaging and segmentation. *Comput. Geosci.* **50**, 25–32 (2013).
20. Blunt, M. J. *et al.* Pore-scale imaging and modelling. *Adv. Water Resour.* **51**, 197–216 (2013).
21. Bernabé, Y., Li, M., Tang, Y.-B. & Evans, B. Pore space connectivity and the transport properties of rocks. *Oil Gas Sci. Technol. Rev. d'IFP Energies Nouv.* **71**, 50 (2016).
22. Tang, Y. B. *et al.* Pore-scale heterogeneity, flow channeling and permeability: network simulation and comparison to experimental data. *Phys. A Stat. Mech. Appl.* **535**, 122533 (2019).
23. Bultreys, T., De Boever, W. & Cnudde, V. Imaging and image-based fluid transport modeling at the pore scale in geological materials: a practical introduction to the current state-of-the-art. *Earth-Sci. Rev.* **155**, 93–128 (2016).
24. Aghaei, A. & Piri, M. Direct pore-to-core up-scaling of displacement processes: dynamic pore network modeling and experimentation. *J. Hydrol.* **522**, 488–509 (2015).

25. Saxena, N. *et al.* References and benchmarks for pore-scale flow simulated using micro-CT images of porous media and digital rocks. *Adv. Water Resour.* **109**, 211–235 (2017).
26. Miao, X., Gerke, K. M. & Sizonenko, T. O. A new way to parameterize hydraulic conductance's of pore elements: a step towards creating pore-networks without pore shape simplifications. *Adv. Water Resour.* **105**, 162–172 (2017).
27. Bondino, L., Hamon, G., Kallel, W. & Kac, D. Relative Permeabilities from simulation in 3D rock models and equivalent pore networks: critical review and way forward1. *Petrophysics* **54**, 538–546 (2013).
28. Baychev, T. G. *et al.* Reliability of algorithms interpreting topological and geometric properties of porous media for pore network modelling. *Transp. Porous Media* **128**, 271–301 (2019).
29. Gerke, K. M. *et al.* Improving watershed-based pore-network extraction method using maximum inscribed ball pore-body positioning. *Adv. Water Resour.* **140**, 103576 (2020).
30. Barsi-Andreeta, M., Lucas-Oliveira, E., de Araujo-Ferreira, A. G., Trevizan, W. A. & Bonagamba, T. J. Pore network and medial axis simultaneous extraction through maximal ball algorithm. Preprint <https://arxiv.org/abs/1912.04759> (2019).
31. Gostick, J. T. Versatile and efficient pore network extraction method using marker-based watershed segmentation. *Phys. Rev. E* **96**, 1–15 (2017).
32. Gostick, J. *et al.* PoreSpy: a python toolkit for quantitative analysis of porous media images. *J. Open Source Softw.* **4**, 1296 (2019).
33. API RP40 in *Recommended practices for core analysis* (American Petroleum Institute, 1998).
34. Tanikawa, W. & Shimamoto, T. Klinkenberg effect for gas permeability and its comparison to water permeability for porous sedimentary rocks. *Hydrol. Earth Syst. Sci. Discuss.* **3**, 1315–1338 (2006).
35. Klinkenberg, L. J. The Permeability of Porous Media to Liquids and Gases in *Drill. Prod. Pract.* (American Petroleum Institute, 1941).
36. Buades, A., Coll, B. & Morel, J.-M. Non-local means denoising. *Image Process Online* **1**, 208–212 (2011).
37. J. Darbon, A. Cunha, T. F. Chan, S. Osher and G. J. Jensen, Fast Nonlocal Filtering Applied To Electron Cryomicroscopy, *5th IEEE International Symposium on Biomedical Imaging: From Nano to Macro*, Paris, pp. 1331–1334 (2008).
38. Schindelin, J. *et al.* Fiji: an open-source platform for biological-image analysis. *Nat. Methods* **9**, 676–682 (2012).
39. Immerkær, J. Fast noise variance estimation. *Comput. Vis. Image Underst.* **64**, 300–302 (1996).
40. Ridler, T. W. & Calvard, S. Picture thresholding using an iterative selection method. *IEEE Trans. Syst. Man, Cybern.* **8**, 630–632 (1978).
41. Hoshen, J., Berry, M. W. & Minser, K. S. Percolation and cluster structure parameters: the enhanced Hoshen-Kopelman algorithm. *Phys. Rev. E* **56**, 1455–1460 (1997).
42. Telea, A. & Vilanova, A. A Robust Level-Set Algorithm for Centerline Extraction. In *Proceedings of the Symposium on Data Visualisation*, 185–194 (Eurographics Association, 2003).
43. Niblack, C. W., Capson, D. W. & Gibbons, P. B. Generating Skeletons and Centerlines from The Medial Axis Transform. In *Proceedings of 10th International Conference on Pattern Recognition* vol. I, 881–885 (1990).
44. Gostick, J. *et al.* OpenPNM: a pore network modeling package. *Comput. Sci. Eng.* **18**, 60–74 (2016).

Acknowledgements

E.L.O., M.B.A. and T.J.B. acknowledge National Council for Scientific and Technological Development (CNPq), Grants (140215/2015-8), (153627/2012-3) and (308076/2018-4), respectively. M.B.A. and T.J.B. acknowledge Centro de Pesquisa e Desenvolvimento Leopoldo Américo Miguez de Mello (CENPES/Petrobras) Grants (2014/00389-8, 2015/00416-8) and (2014/00389-8), respectively. R.F.N. and M.S. acknowledge Alexandre Ashade, Peter Bryant, William Candela, Ítalo Nievinski, Giulia Coutinho (IBM Research) for their contributions to earlier versions of the CNM algorithm, Ricardo Ohta (IBM Research) for help with the 3D rendered images, and Ronaldo Giro and Michael Engel (IBM Research) for helpful discussions and insights. The authors would like to thank T.J.B. (USP) and Ulisses Mello (IBM Research) for making the collaboration between these institutions possible.

Author contributions

M.S. and T.J.B. conceived the work. W.A.T. performed porosity and permeability measurements at lab scale. E.L.O. acquired X-ray microtomography images. H.B. developed the capillary network extraction algorithm. R.F.N. and M.B.A. performed the computer simulations and data analysis. R.F.N. and M.S. wrote the paper with input from all the co-authors.

Competing interests

The authors declare no competing interests.

Additional information

Supplementary information The online version contains supplementary material available at <https://doi.org/10.1038/s41598-021-90090-0>.

Correspondence and requests for materials should be addressed to R.F.N. or M.B.S.

Reprints and permissions information is available at www.nature.com/reprints.

Publisher's note Springer Nature remains neutral with regard to jurisdictional claims in published maps and institutional affiliations.



Open Access This article is licensed under a Creative Commons Attribution 4.0 International License, which permits use, sharing, adaptation, distribution and reproduction in any medium or format, as long as you give appropriate credit to the original author(s) and the source, provide a link to the Creative Commons licence, and indicate if changes were made. The images or other third party material in this article are included in the article's Creative Commons licence, unless indicated otherwise in a credit line to the material. If material is not included in the article's Creative Commons licence and your intended use is not permitted by statutory regulation or exceeds the permitted use, you will need to obtain permission directly from the copyright holder. To view a copy of this licence, visit <http://creativecommons.org/licenses/by/4.0/>.